Experimental regression rate profiles of stepped fuel grains in Hybrid Rocket Engines

Christopher Glaser, R. Gelain, A.E.M. Bertoldi, Quentin Levard, J. Hijlkema, J.-Y. Lestrade, P. Hendrick, Jérôme Anthoine

Acta Astronautica 204 (2023) 186–198

Contents lists available at ScienceDirect

Acta Astronautica

journal homepage: www.elsevier.com/locate/actaastro

Research paper

Experimental regression rate profiles of stepped fuel grains in Hybrid Rocket Engines

C. Glaser [a,*], R. Gelain [b], A.E.M. Bertoldi [b], Q. Levard [a], J. Hijlkema [a], J.-Y. Lestrade [a], P. Hendrick [b], J. Anthoine [a]

[a] ONERA/DMPE, Université de Toulouse, F-31410 Mauzac, France
[b] Aero-Thermo-Mechanics Department, Université Libre de Bruxelles, 50 Avenue F. D. Roosevelt, 1050 Brussels, Belgium

ARTICLE INFO

Keywords:
Hybrid rocket engine
Regression rate enhancement
Backward and forward facing step
Fuel grain design
CH* chemiluminescence
Longitudinal slicing method

ABSTRACT

In this work, we assess the impact of stepped hybrid rocket solid fuel grains on the performance of the engine. The influence of Forward Facing Steps (FFS) and Backward Facing Steps (BFS) on the regression rate is analysed on two different cylindrical motors and one slab burner with optical access. Accessible post-processing allows to quantify the local regression rate profiles induced by the steps for the cylindrical motors. For the slab burner, novel image processing approaches enable the authors to correlate the findings of the cylindrical motors precisely to the visual inspection of the slab burner. Using two different cylindrical motors with different fuel grain lengths stressed the importance of the total motor length on the effect of the steps. Shorter grains (118 mm) exhibit higher regression rates for FFS than for BFS (+41.3% versus +15.7%), whereas longer motors (500 mm) profit more from BFS than FFS (+26.3% versus ±0%). Moreover, using three different oxidizers (nitrous oxide, hydrogen peroxide and gaseous oxygen) and two different fuels (high density polyethylene and paraffin) at different O/F ratios, we showed that the beneficial properties of steps are valid for numerous configurations. This would allow the employment of stepped geometries to a variety of existing motors. Finally, the authors propose the possibility to approximate fuel grain designs by a set of multiple steps.

1. Introduction

Hybrid Rocket Engines (HREs) are a promising technology to achieve a cheaper, more sustainable and competitive access to space. So far, liquid rocket engines and solid rocket motors have been preferred over HREs for launcher applications. This is due to the low maturity of HREs, as well as challenges related to low regression rate, combustion inefficiency, oxidizer-to-fuel ratio (O/F) shift during operation and high residual inert mass [1]. Nonetheless, in recent years, the new space market calls also for cheap micro- and nano-launchers. HREs could help to fill this niche given their advantages (e.g. high performance, intrinsic safety, throttle-ability, flexibility and low cost), provided that some of the disadvantages are being solved. Starting in 2010, the number of publications on HREs increased considerably [2], proving the rising interest in the potential capabilities of HREs.

In previous work [3,4], we proposed to distribute a set of BFS and FFS (in the form of cylindrical fuel grains with varying inner diameter) along any predefined optimized profile as depicted in Fig. 1. This way, three major advantages are anticipated:

1. Instead of 3D-printing complex fuel geometries, the fuel port profiles can now be approximated by a finite number of fuel cylinders with varying inner diameter.
2. The fuel port still exhibits the benefits its fuel port profile was optimized for, e.g., lower O/F shift during operation.
3. The set of steps increase turbulence, mixing, heat transfer and, thus, enhance the overall regression rate.

This article serves as a direct continuation of the preliminary work presented in [4]. Up to this point, no information on the different mechanisms of FFS and BFS in HREs is available to the knowledge of the authors. This makes the endeavour to distribute multiple steps along a profile difficult. In order to gain further insight into the phenomenon of regression rate enhancement through BFS and FFS, three experimental campaigns are carried out on three different lab-scale HREs both at Université Libre de Bruxelles (ULB) and at ONERA. The first campaign, using nitrous oxide (N_2O) and High-Density Polyethylene (HDPE) as propellants with a grain length of 118 mm, and the second campaign using hydrogen peroxide (H_2O_2) and HDPE with a grain length of 500 mm. In doing so, we are able to assess the impact on the steps over

* Corresponding author.
E-mail address: christopher.glaser@onera.fr (C. Glaser).

https://doi.org/10.1016/j.actaastro.2022.12.045
Received 14 December 2022; Accepted 29 December 2022
Available online 3 January 2023

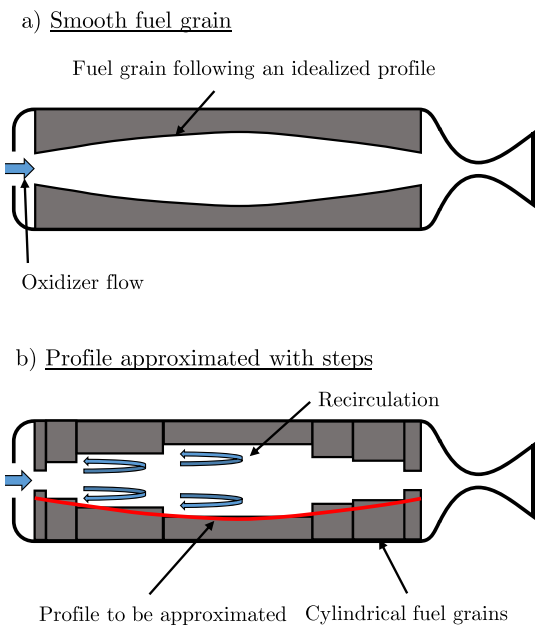

Fig. 1. Approximation of fuel port profiles as proposed in [3,4].

Table 1
Overview of test campaigns.

Campaign	Motor	Institution	Oxidizer	Fuel	Motor type
ULB	ULB-HRM [5]	ULB	N_2O	HDPE	Cylindrical
HYCAT	HYCAT [6]	ONERA	H_2O_2	HDPE	Cylindrical
MOUETTE	MOUETTE [7]	ULB	GOX	Paraffin	Slab burner

a broad range of initial conditions, motor geometries and oxidizers. Additionally, to investigate the effect of the steps on the regression rate already during the test, we tested BFS and FFS geometries in a gaseous oxygen (GOX) and paraffin slab burner with optical access, effectively adding a third propellant couple to the test campaigns.

The focus of this article can be summarized as follows: the cylindrical motors will be equipped with fuel grains that consist of either a single FFS or BFS in the centre of the grain. After each test, the fuel grains are investigated and their local regression rate profile as well as the space and time averaged regression rates assessed. Moreover, the tests are compared to no-stepped reference cases to quantify the regression rate enhancement. These campaigns are presented in Section 4. Additionally, with the use of the optical access of the 2D slab burner, the effect of the steps on the HRE flow-field and regression rate is investigated visually already during the test and the results obtained can be correlated to the cylindrical motor campaigns. The 2D step campaign will be explained in Section 5. In Table 1, the three different motors and their characteristics are summarized.

2. Turbulence enhancing devices in the literature

The application of diaphragms, resembling both a FFS and BFS at the same time, and other turbulence and heat exchange enhancing devices in the solid fuel grain have proven to increase both regression rate and combustion efficiency due to the formation of recirculation zones [8]. These zones increase turbulence and mixing as well as heat transfer and, as a consequence, lead to improved performance of the HREs. This effect can also be found near the inlet of injectors, where the local regression is enhanced due to the formation of a recirculation zone [9–11]. In our work, we will concentrate on the effect of diaphragm and step research found in open literature, as well as comparable designs. For an extensive collection of regression rate enhancing techniques through turbulence (among others) the reader is referred to the work in Ref. [8].

The first recorded use of a diaphragm in a flight tested hybrid rocket motor was in the LEX (Lithergol Experimental) rocket of ONERA in the 1960s to promote mixing and regression rates [12]. In 1972, Gany and Timnat [13] increased the regression rate of a polyester HRE around 50% by using a diaphragm in the centre of the fuel grain. Grosse [14] researched extensively the use of diaphragms with different cross-section shapes in paraffin based motors and observed regression rate increments of 84% downstream a 4-holed diaphragm. Dinesh and Kumar [15] exploited experimentally the fact that the regression rate enhancing effect of diaphragms relates directly to the recirculation zone length. For this reason, they distributed multiple diaphragms inside the fuel port to maintain the enhancing effect of the diaphragms throughout the fuel grain length. They found an ideal spacing for their motor of 2.7 times the recirculation zone length.

As for steps, Korting et al. [16] observed in 1987 increased regression rates directly after a BFS in their HRE. Locally, the fuel consumption almost doubled, which was attributed to the enhanced mixing due to the recirculation zone behind the step. Lee et al. [17] used a single BFS inside the fuel grain, thereby decreasing combustion instabilities and increasing the regression rate 50% downstream the BFS. Sakashi et al. [18] tested a concave–convex design (effectively resembling a sequence of BFS and FFS) and observed 70–100% increased regression rates. Later, Kumar and Joshi [19] also created a grain of alternating steps using cylinders with two different inner diameters and increased the average regression rate between 30 and 55%. Kamps et al. [20] have employed a single BFS in their motor to increase mixing after the step. Although this was not the main goal of the study, they noted a decrease in regression rate directly after the step, however, after this initial decline, the regression rate increased again, presumably above the base-line. To use a set of steps with different heights and widths to follow a predefined profile or any other geometry has neither been proposed nor tested to the knowledge of the authors.

Two noteworthy other motor designs that increase the turbulence by disturbing the flow are the CAMUI (Cascaded Multistage Impinging-Jet) [21] engine and the segmented grain of Tian et al. [22]. The CAMUI engine consists of multi-port fuel grain segments that are separated by a fuel spacer to promote mixing. Moreover, the fuel grains are rotated 90° against each other. Due to this, the flow is mixed inside the fuel spacers and then enters the next grain segment (which can be interpreted as a step) with higher turbulence and mixing. The regression rate inside the fuel ports is therefore increased by up to 115% as compared to classical fuel ports engines [23]. The multi-segmented design of Tian et al. [22] follows a similar path and consists of multiple fuel grains with a relative angular displacement and mixing chambers in between. If two segments with three fuel ports in the second grain are used, the regression rate of the ports of the grain downstream increases by 20%.

3. Experimental estimation of regression rate

In literature, several methods to estimate the regression rate after the burn are used. Basically, the final diameter (D_f) of the fuel grains after the test needs to be determined to estimate the (time and space averaged) regression rate ($\dot{r}$) with the help of the initial diameter (D_0) and burn time (t_b):

$$\dot{r} = \frac{D_f - D_0}{2t_b}. \tag{1}$$

However, obtaining the final diameter after the fuel grains have been fired can be rather difficult. For this work, we employ two different techniques to estimate the final diameter and, thus, the time averaged regression rate. The first is the mass loss method to obtain the time and space averaged regression rates, and the second a longitudinal slicing method to assess the local regression rate profiles. In the following sections, both strategies are explained and their susceptibility to measurement errors assessed.

3.1. Mass loss method

The commonly used mass loss method allows to estimate the final diameter based on the fuel mass consumed during the burn. Assuming uniform, cylindrical consumption, and knowing the fuel density (ρ_f) and grain length (L_g), the final diameter amounts to [24]:

$$D_f^2 = \frac{4\Delta m_f}{\pi \rho_f L_g} + D_0^2 \,, \tag{2}$$

with Δm_f being the difference in fuel weight obtained by weighing the grain before and after the burn. Using Eq. (1), the time and space averaged regression rate can be now obtained. While this method is convenient to employ, the main downside is the assumption of a uniform, cylindrical fuel consumption which allows no conclusions on the (local) regression rate profile along the grain axis. The longitudinal slicing method introduced in the next section, on the other hand, allows also the determination of the local regression rate profiles.

3.2. Longitudinal slicing method

After the experimental campaign, the fuel grains are cut along their longitudinal axis. Next, the halves are digitized with a standard office scanner. With image processing tools such as *Fiji* [25], the local final inner diameter $D_f(x)$ of the fuel grain can be measured, assuming locally axisymmetric fuel regression. Knowing the initial diameter, the temporally averaged local regression rate can be easily derived using the expression:

$$\dot{r}(x) = \frac{D_f(x) - D_0(x)}{2t_b} \,. \tag{3}$$

Moreover, the space and time averaged regression rate (over any interval $[x_0, x_1]$ of interest) can be calculated using:

$$\dot{r} = \frac{1}{x_1 - x_0} \int_{x_0}^{x_1} \dot{r}(x)\, dx \,, \tag{4}$$

and the average final diameter can be obtained with a simple integration:

$$D_f = \frac{1}{x_1 - x_0} \int_{x_0}^{x_1} D_f(x)\, dx \,. \tag{5}$$

Likewise to the mass loss method, the slicing approach is rather easy to apply. Nonetheless, special care has to be taken concerning the accuracy of the cut. There are two potential sources of errors in the slicing approach. The first is the parallel displacement of the cut from the axis. Fig. 2 illustrates the relative error in the measurement of the diameter (measured diameter versus real diameter) when the line of attack of the cut is displaced parallel to the grain axis. It becomes obvious that for large port fuel grains the relative error is well below a threshold of 5% which was set as the maximum allowed error by us. For smaller fuel ports, the error becomes more pronounced. However, the discrepancy stays below 5% for displacements of 4 mm or less, which gives sufficient margin to apply the method. The grains presented in the ULB campaign have been processed with a maximum displacement of 3 mm in the least accurate case, which for the concerning grain diameter above 50 mm translates to an error of around 1%. For the HYCAT campaign, the displacement error thanks to more precise machining could be held well below 0.5 mm, resulting in a negligible error of below 1%.

Similar considerations of accuracy can be applied to the angular displacement of the saw. Fig. 3 displays possible error values for different fuel port diameters and fuel grain lengths. Even for the small fuel grain port diameters of the 118 mm grain length (typical length of the ULB motor), all angular displacements of 4 degree and less give almost negligible relative measurement errors. For longer fuel grains (such as the ones used with the HYCAT motor at ONERA, where the total fuel grain is composed of two grains of 240–250 mm each), the error gets more pronounced, especially for the small fuel ports. However, during

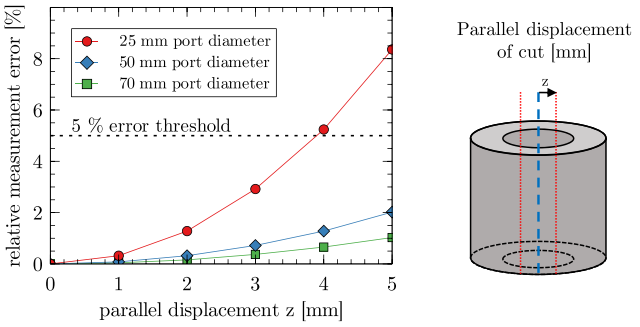

Fig. 2. Parallel displacement error.

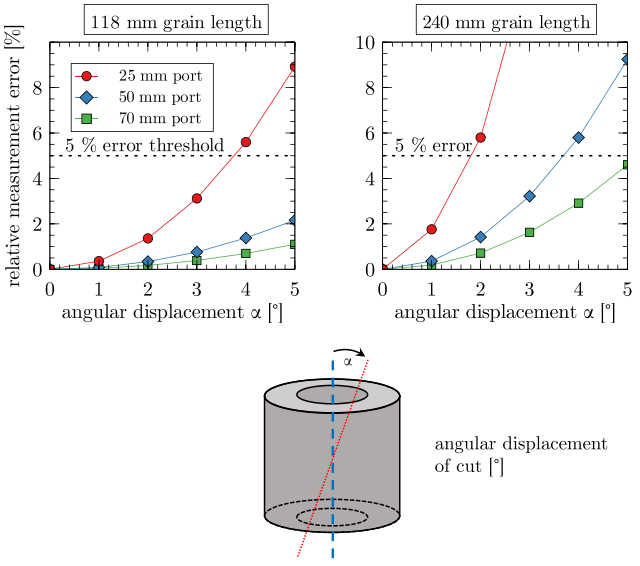

Fig. 3. Angular displacement error.

the test campaigns in this study, the angular displacement even with standard equipment was well below 2 degrees (in the case of the ULB campaign) and below 1 degree for the HYCAT campaign. It is to be stressed that angular displacements change the fuel port shape after the cut, as the measured diameters at the ends of the axis are smaller than the one in the middle. For small port grains with higher lengths and imprecise equipment, this effect also needs to be considered.

3.3. Marxman law and average oxidizer mass flux

In this article, the classic Marxman law [26] will be used to evaluate time and space averaged regression rates. The law is written as:

$$\dot{r} = a \cdot G^n \,, \tag{6}$$

where $\dot{r}$ is the regression rate in mm/s, G the total mass flux and a, n are constants that can be determined experimentally. Usually, the exponents are dependent on propellant couple, initial conditions and motor geometry. Since the total mass flux G is not directly measurable, the oxidizer mass flux G_{ox} is often used instead. It is defined as:

$$G_{ox} = \frac{4\dot{m}_{ox}}{\pi D^2} \,, \tag{7}$$

with $\dot{m}_{ox}$ and D being the oxidizer mass flow and the fuel port diameter respectively. When it comes to define an average G_{ox} for the Marxman law, the two most utilized possibilities are the following [27]: either the mass flux is averaged between the initial and final values of G_{ox}, or

Table 2
Cylindrical test cases.

Campaign	Motor	Ref. Cases	BFS	FFS
ULB	ULB-HRM	4	3	3
HYCAT	HYCAT	4	1	1

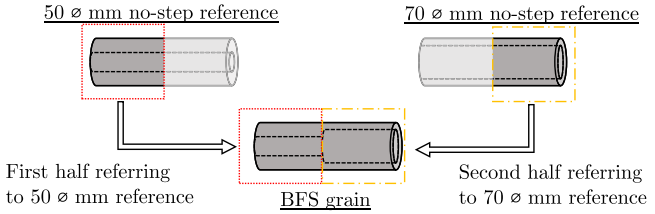

Fig. 4. Visualization of two sub-references of a BFS grain.

the mass flux is averaged using an average fuel port diameter (D_{avg}), calculated as:

$$D_{avg} = \frac{D_0 + D_f}{2} . \tag{8}$$

Interestingly, due to the non-linearity of the definition of the mass flux G_{ox}, these methods yield different results for the mass fluxes and, thus, for the Marxman fit. Karabeyogulu et al. [27] concluded analytically that the average fuel port diameter approach of Eq. (8) leads to a smaller error and it is thus adopted in this article. Summarizing, the average oxidizer mass flux can be written as:

$$G_{ox,avg} = \frac{16\dot{m}_{ox}}{\pi(D_0 + D_f)^2} , \tag{9}$$

with D_f being the final diameter either estimated with the mass loss method or the longitudinal slicing method that was explained in Sections 3.1 and 3.2; depending on the use-case.

4. Cylindrical test campaigns

The objective of the cylindrical test campaigns is to investigate the effect of BFS and FFS on the (local) regression rate over a range of propellant combinations and motor geometries. The ULB campaign consists of four reference cases without steps, two with five seconds burn time and two with ten seconds burn time. Three BFS and FFS cases each are compared to these reference cases. For the HYCAT campaign, four reference cases and one FFS and BFS case each are conducted, as summarized in Table 2.

Before the results of the cylindrical campaigns can be presented and discussed, it is necessary to define the meaning of a 'reference case'. In a stepped case, the fuel port diameter is not constant, as it changes before and after the step and, therefore, the mass flux varies accordingly. Given the high dependency of the regression rate on the mass flux, the stepped case needs to be compared to the no-step reference with the same diameter before the step and consequently with a different diameter after the step. This approach is depicted in Fig. 4: the stepped cases are compared to two sub-references. For example, in the ULB motor, a BFS case is compared to the 50 mm port diameter reference in the first half and to a 70 mm port diameter reference in the second half (after the step).

4.1. The ULB test campaign

The ULB test campaign has been carried out on the ULB-ATM HRE [5,28], which has been designed to provide 1 kN of thrust for a burning time of 10 s, initially using liquid N_2O as oxidizer and paraffin wax as a fuel. The nitrous oxide is pressurized at 60 bar with nitrogen and the average chamber pressure during the test campaign yielded around 16 bar. For our studies, we decided to use HDPE as fuel instead of paraffin, because the fuel consumption of paraffin could be too fast to assess the step in the fuel grains after the tests.

It is to be noted that changing the fuel to HDPE is anticipated to have a rather dominant effect on the O/F values (as can be seen in Table 3). This is due to the fact that the motor was initially optimized for paraffin fuels. Therefore, the fuel grain is rather short (118 mm), as paraffin has approximately 3–4 times the regression rate of HDPE [29]. The short grain length together with the lower regression rates of polymer fuels leads to an untypical high O/F of around 16–26 when the ideal O/F of N_2O and HDPE is around 8. This signifies an oxidizer rich mixture. These rich mixtures will have significant effects on nozzle erosion, flame temperature and specific impulse [30,31]. Nonetheless, since we assume the high O/F does not have a qualitative impact on the shape of the regression rate profiles (which is the characteristic of interest in this campaign), we opted for HDPE.

Pressure measurements can be acquired in the engine and in the feed system. For the analysis of combustion instabilities, a piezoelectric pressure transducer can be used in the post-chamber as well. K-type thermocouples allow to measure the temperature of the oxidizer in the lines, and two load cells are used to measure the thrust of the engine and the variation of oxidizer mass in the tank. To estimate the N_2O mass flow, the weight loss of the N_2O tank is related to the burn time of the motor. For the injection, a showerhead injector is used, which yielded N_2O mass flow rates between 0.354 and 0.537 kg/s in our case. The engine parameters and the design process are described in more detail in Refs. [5,28].

Based on a previous numerical study on the HYCAT motor at ONERA [3], where step heights over 10 mm seem to saturate the effect of steps, the step heights are fixed to 10 mm. This signifies a diameter difference of 20 mm for the ULB campaign. In order to facilitate the production of the fuel grains, only two fuel port diameters (50 mm and 70 mm) are considered. A total of 11 hot fire tests (T1–T11) have been conducted with the ULB motor. During T5, due to a leak in the combustion chamber, the ignition phase was abnormally long, that is why we do not consider T5 for this analysis. A small leak has been identified also in T4. However, this did not lead to ignition problems, but higher incertitudes concerning the oxidizer mass flow rate, chamber pressure and burn time. Moreover, T7 exhibited anomalies during the burn (chamber pressure and thrust readings dropping rapidly during the test and suddenly increasing again). For this reason we decided to extend the ULB campaign with T10 and T11. However, we were able to recover the regression rate profiles from T4 and T7 and will include them in the section about the regression rate profiles (but not the space and time averaged comparison) to prove consistency.

4.2. Experimental results of the ULB campaign

The results of the test campaign will be exploited in two ways. First, the local regression rate profiles along the fuel grain surface will be examined to confirm that steps can increase the regression rates and to find explanations for the mechanisms behind this behaviour. Subsequently, the space and time averaged regression rates will be compared and analysed for all the cases to derive an indication into the effectiveness of BFS and FFS. The test conditions are presented in Table 3.

4.2.1. Surface profiles of ULB campaign

The surface profiles are obtained with the slicing method explained in Section 3.2 and three post-firing scans are presented in Fig. 5. Fig. 6 illustrates the final diameter versus the initial diameter of the BFS tests (T4, T6 and T10). The position of the step is at zero axial position, and only the grain surface 40 mm before and after the step is considered in all following figures. This choice allows to exclude the burning of the lateral fuel surfaces at the beginning and the end of the grain as well as the injector effects at the beginning of the fuel grain. The diameter value displayed in the y-axis is the outer grain diameter (D) minus the

Table 3
Overview of ULB test conditions.

Test	Config.	t_b [s]	$\dot{m}_{ox}$ [kg/s]	O/F [-]	G_{ox} [kg/m^2 s]	$\dot{r}$ [mm/s]	Δ m_f [g]
T1	Ref.	9.90	0.354	22.21	77.85	0.61	159.3
T2	Ref.	10.00	0.403	18.52	140.24	1.05	217.4
T3	FFS	4.50	0.468	16.10	137.68	1.29	130.8
T4	BFS	3.97	0.473	20.91	146.67	1.03	90.0
T6	BFS	5.11	0.537	19.47	156.12	1.21	141.2
T7	FFS	5.99	0.483	21.05	140.82	1.01	137.3
T8	Ref.	5.06	0.529	26.26	122.95	0.79	102.0
T9	Ref.	5.81	0.496	19.14	190.18	1.31	150.6
T10	BFS	4.46	0.528	18.75	156.32	1.25	125.5
T11	FFS	4.35	0.518	15.42	149.70	1.47	146.1

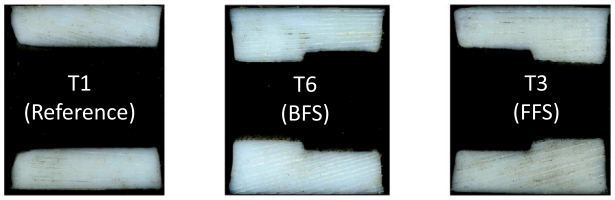

Fig. 5. Scans of fuel grains after test. Oxidizer flow from left to right.

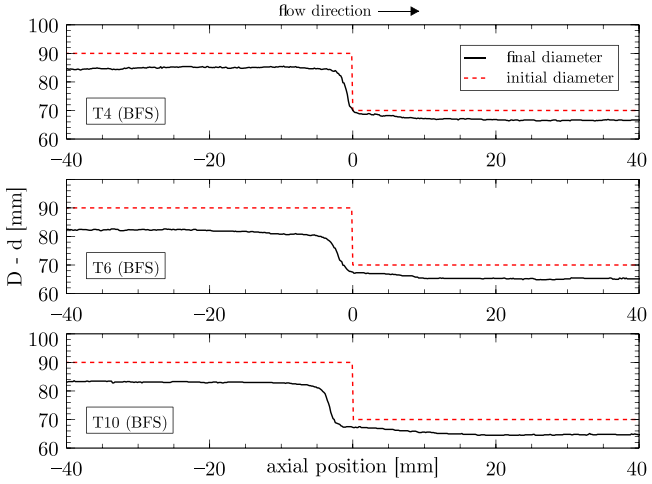

Fig. 6. Initial vs. final diameter of BFS cases.

inner diameter (d) to allow for a more convenient interpretation of the figure.

Looking at the final diameters in Fig. 6, it appears that with increasing burn time, the steps become more and more rounded. Before the step, the regression seems to be almost parallel. On the other hand, after the step, a small plateau is visible. This indicates that the local regression rate at this point is lower due to the flame being further away from the surface. After this plateau, however, the regression of the surface is more elevated due to the increased mixing induced by the recirculation zone that forms behind the BFS. This effect has been already anticipated numerically by a parametric study [3] on the HYCAT motor of ONERA. The flowfield of a BFS inside an HRE from this study is illustrated in Fig. 7, where the distance of the flame to the surface after the step and the recirculation zone becomes apparent.

This common trend becomes more clear when compared with the regression rate profiles calculated using Eq. (3). The results for the BFS are displayed in Fig. 8. The black data-set is the BFS surface profile of the BFS test cases. The red and green data are the corresponding no-step reference cases at 5 and 10 s burn time. To recall, a reference case for BFS is composed of a 50 mm diameter port no-step grain in the first half, and a 70 mm diameter no-step grain in the second half (refer also

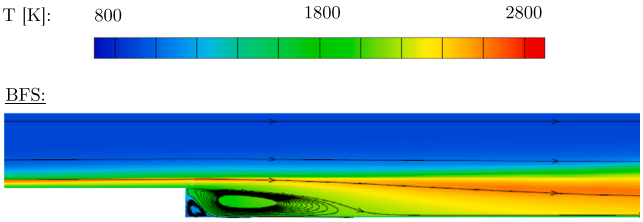

Fig. 7. Flow-field of axisymmetrical BFS simulation.

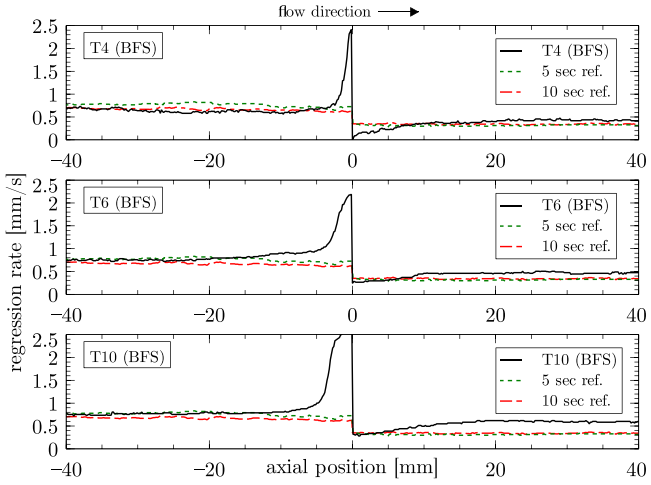

Fig. 8. Regression rate profile of BFS cases. (For interpretation of the references to colour in this figure legend, the reader is referred to the web version of this article.)

to Fig. 4). In this way, the regression rates of approximately the same G_{ox} are compared among each other.

For T4, the regression rate before the step is almost identical to the reference cases. For T6, however, the regression rate increases already before the step. This is due to the (lateral) progression of the step also visible in Fig. 6: the step profile gets smoother and changes its shape, leading to a 'discontinuity' in the regression rate estimation at the initial position of the step and to a higher regression rate before it. Directly after the step, the regression rate exhibits a minimum because of the flame being more detached from the fuel surface (refer also to Fig. 7). After a short distance, however, the regression rate increases when compared to the reference cases due to the reattachment of the flow and enhanced mixing and heat transfer induced by the recirculation zone. The 'discontinuity' in the regression rate is even more pronounced when looking at the profile of T10 in Fig. 8. Here, the local regression rate directly before the step is higher due to the (lateral) progression of the step. It is to be noted that all three BFS cases show exactly the same qualitative trend in their profile, suggesting a reliable reproducibility.

Turning to the FFS cases, Fig. 9 shows the diameter profiles of the FFS fuel grains. The longitudinal progression of the step from its initial position is again visible. Interestingly, shortly before the step, the profile is more regressed, forming a cavity. This hints at increased regression rate due to the positive effects of the recirculation zone that forms before the FFS. Moreover, directly after the FFS, another area of higher regression can be seen (visible for T3 and T11 immediately after the step). This area of more regressed fuel can be related to the length of the recirculation zone that forms after the FFS. Inside this recirculation zone mixing and turbulence are increased. Together with increased heat transfer to the fuel surface, these effects increase the regression rate locally. Fig. 10 depicts the numerical flow-field inside a HRE with a FFS as obtained from [3]. Here, the two recirculation zones and the distance of the flame to the grain surface before the step are visible.

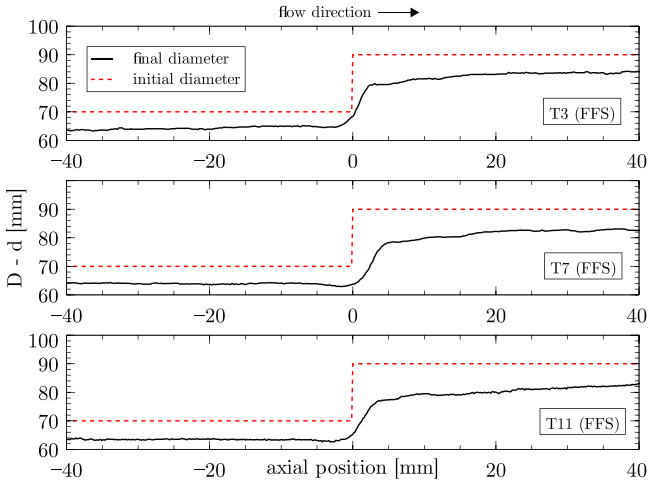

Fig. 9. Initial vs. final diameter for FFS cases.

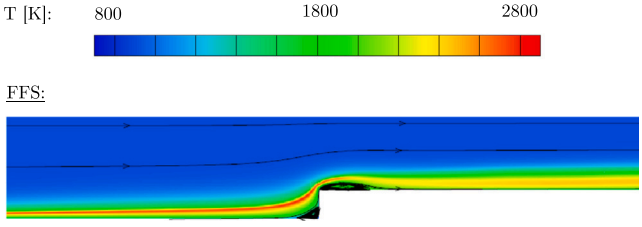

Fig. 10. Flow-field of axisymmetrical FFS simulation.

The positive effects of the recirculation zone induced by the steps become more evident when considering the regression rate profiles of the FFS cases in Fig. 11. Here, the regression rate of the FFS cases is plotted alongside the two respective reference cases. The two distinct peaks of regression rate due to the recirculation zones become apparent. For the zone before the step, it is a small distinct peak (especially for T7), whereas for the zone behind the step it is rather an area of increased regression rate.

Compared to the reference cases, the regression rate profiles in Fig. 11 before the step follow approximately the same trend. However, quantitatively the stepped cases have higher regression rates before the step (most pronounced in T11). This fact is rather due to uncertainties in mass-flow rate than to the effect of the step, given the fluctuations in oxidizer mass-flow during the different tests.

Directly after the FFS, however, the regression rate for the stepped cases is considerably higher. Interestingly, the regression rate value descends again to the level of the reference cases, with the exception of T11 that has an overall higher regression rate already before the step. However, as visible in the other FFS cases (also later in the HYCAT campaign) and based on the numerical study in [3], we can assume that the regression rate of T11 approaches its respective reference case asymptotically. This suggests that the effect of the recirculation zone for the FFS cases is limited in its length and diminishes with increasing distance to the step. This is contrary to what has been observed for the BFS cases (recalling Fig. 8) where the effect of the recirculation zone increased the regression rate constantly over the reference cases for the remaining length of the fuel grain. Likewise to the BFS cases, all FFS results follow qualitatively the same trend, again showing consistency in the positive effects of steps on the enhancement of the regression rate in HREs.

To conclude, the impact of BFS and FFS on the regression rate can be observed experimentally in the regression rate profiles. The recirculation zone behind the BFS increases the regression rate after the step considerably when compared to the reference cases and fully

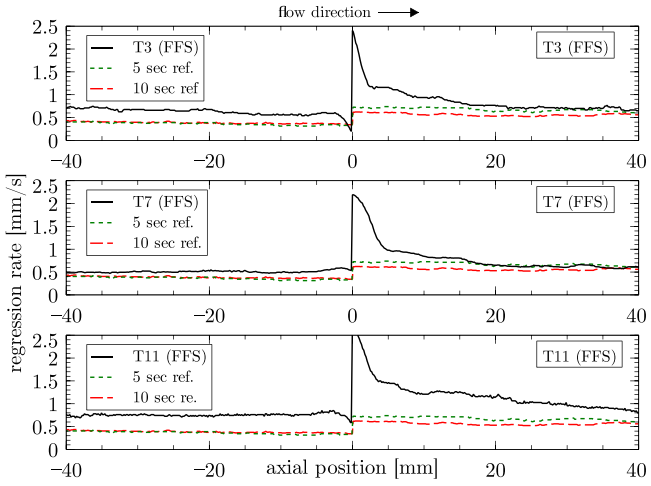

Fig. 11. Regression rate profile of FFS cases. (For interpretation of the references to colour in this figure legend, the reader is referred to the web version of this article.)

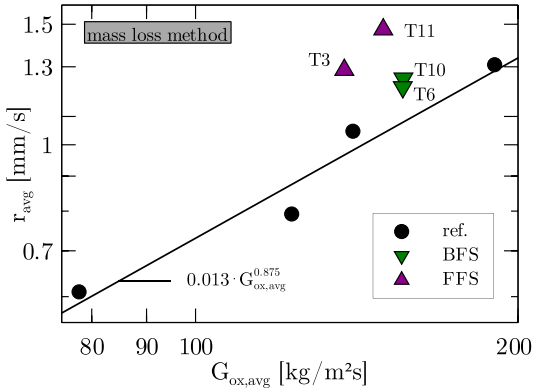

Fig. 12. Averaged regression rate over whole fuel grain length.

over the remaining fuel grain length. For the FFS cases, the increase of the regression rate is visible before and after the step, however, the peak in regression rate decreases with distance downstream the FFS and descends to the level of the reference cases, hinting at the fact that the FFS have a very high, distinct effect directly after the step and it decreases with distance downstream the step. This behaviour will further be investigated in Section 4.3.

4.2.2. Time and space averaged regression rate of ULB campaign

In the previous section on local surface profiles, the effect of the steps could be evaluated locally. Nonetheless, in order to understand the effect of FFS and BFS over the total grain length, we will concern ourselves with the space and time averaged regression rates following the approach presented in Section 3.3.

The space and time averaged regression rate is plotted in Fig. 12. The black line represents the Marxman [26] fit in the form of $\dot{r} = a \cdot G^n$; only for the reference cases. With the help of these data we can evaluate the effect of the steps on the whole fuel grain.

In total, the regression rate of the FFS cases lies above the reference trend (about 41.3% for the case of T11). For the BFS cases, they both remain also above the reference line (around 15.7% increase) mainly due to the dominant increase in regression rate for the second half of the grain. This signifies that for the ULB campaign the FFS cases have significantly higher impact on the regression rate. This observation can be explained by recalling Figs. 8 and 11. The increase in regression rate due to FFS is very pronounced but limited in its area of influence. For the BFS cases, on the other hand, the effect of the step is less

pronounced but very consistent for the full grain downstream the step. This hints at a strong connection between total fuel grain length and the impact of steps. The ULB grains are rather short (around 118 mm). This signifies that the strong peak after the FFS has a considerable impact on the space averaged regression rate, as the area of influence of the FFS is in the same order of magnitude as the remainder of the fuel grain length downstream the step.

For the BFS cases it is the inverse. Directly after the step, there is a strong decrease in regression rate due to the flame being further away from the fuel surface. It is not until the boundary layer redevelops with higher turbulence and mixing induced by the step, that the regression rate of the BFS cases overtakes the reference cases. However, given the short length of the ULB grains, the smaller but very consistent effect of the BFS cannot increase the regression rate as much as the FFS cases did. This strong indicator of the importance of the fuel grain length for steps will be discussed in Section 4.4 with the help of the longer fuel grains of the HYCAT campaign (500 mm).

To conclude, it has been shown that both BFS and FFS have the potential to considerably increase the total regression rate. In this first test campaign, the cases supported the assumption of increased regression rates due to BFS and FFS and were hinting at a strong correlation of the effect of the steps to the total fuel grain length. For all six stepped cases, the qualitative trend is reproducible.

4.3. The HYCAT campaign

During the ULB campaign, strong indications towards the importance of fuel grain length were discovered. For this reason, we extended the investigation of stepped geometries to longer fuel grains. With this, we can potentially reinforce this initial assumption while also proving reproducibility of the results on a completely different motor design with a different propellant couple.

The test campaign at ONERA was carried out on the HYCAT (*HYbrid with CATalyzer*) motor [6,32]. It uses H_2O_2 (87.5%) and HDPE as propellants. The hydrogen peroxide is decomposed over a catalyst bed and injected into the combustion chamber. The oxidizer mass flow used for our tests is set to approximately 0.35 kg/s, measured with a Coriolis mass flow meter. Four piezoelectric pressure probes measure the chamber pressure in the pre- and post-chamber, and the temperature upstream the axial injector is recorded as well. The length of the engine can be adjusted thanks to its modular design, allowing for a wide range of fuel grain lengths. In this test campaign, the length was chosen to be 500 mm to reach O/F values closer to the stoichiometric value of around 7. Moreover, the length is around 4.5 times higher than for the ULB campaign, which enables us to investigate the impact of grain length on the effect of steps. The combustion gases are ejected through an ablatively cooled nozzle. In the concerning tests, the engine was operated at around 25 bar chamber pressure leading to thrust ranges of around 700 N, which was measured with the thrust balance the engine is mounted on.

A total of 6 tests (4 reference cases and one FFS and BFS case each) were conducted in a similar fashion to the ULB campaign before. The step height was altered from the ULB campaign to investigate a potential optimal step height of 7.5 mm that was postulated in a numerical study on HYCAT [3], where the optimum was suspected to fall numerically between 5 and 10 mm step height. This yields a 15 mm difference in fuel grain diameter, and, thus, grains of 25 and 40 mm initial diameter have been selected. Two different types of reference cases were used, two with a fuel grain length of 250 mm and two with a total grain length of 500 mm.

4.4. Experimental results of the HYCAT campaign

Similar to the ULB campaign, the results of the HYCAT campaign will be exploited first by assessing their regression rate profile, and consequently by evaluating their time and space averaged regression rate. The test conditions and global results are presented in Table 4.

Table 4
Overview of HYCAT test conditions.

Test	Config.	t_b [s]	$\dot{m}_{ox}$ [kg/s]	O/F [-]	$G_{ox,avg}$ [kg/m^2 s]	$\dot{r}$ [mm/s]	Δm_f [g]
H46	Ref.	9.41	0.303	16.49	371.23	0.77	172.7
H47	Ref.	9.28	0.329	26.10	220.11	0.39	116.8
H48	Ref.	9.65	0.337	7.96	388.02	0.86	408.9
H49	Ref.	9.65	0.348	12.58	228.02	0.42	266.7
H50	FFS	9.60	0.343	10.19	299.37	0.59	322.8
H52	BFS	9.66	0.346	8.84	289.59	0.67	378.2

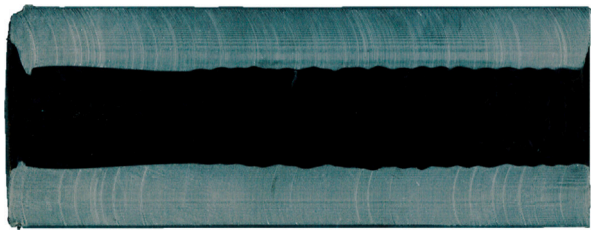

Fig. 13. Post firing scan of first half (250 mm) of H48. Oxidizer from left to right.

4.4.1. Surface profiles of HYCAT campaign

Following the slicing approach presented in Section 3.2, the surface profiles of this campaign are presented here. Additionally, Fig. 13 illustrates a scan of the fuel grain after the test H48.

Starting with the initial and final diameters, Fig. 14 displays the curves for the BFS (top) and FFS (bottom) of the HYCAT campaign. Again, for a more accessible illustration, the y-axis shows the outer grain diameter (D) minus the inner diameter (d). The step position is at 0 mm and the axial position ±175 mm is considered to exclude injector effects and lateral burning of the end surfaces of the grain.

For the BFS in Fig. 14, the diameter regresses rather uniformly as it was also the case for the ULB campaign. After the step, the diameter becomes more rounded and converges into an almost perfect horizontal profile. For the shorter grains of ULB, this convergence into a horizontal state could be speculated, but it was not completely achieved (recall Fig. 6).

Concerning the FFS (lower half of Fig. 14), the longitudinal movement of the step is well visible due to the constant impingement of the hot flow on the FFS surface together with the formation of a recirculation zone. Behind the now progressed FFS, a cavity is visible, indicating the locally increased regression rate due to the formation of the recirculation zone behind the FFS.

Using Eq. (1), and knowing the final diameter of the BFS and FFS cases, the time average local regression rate is obtained and shown in Fig. 15. Following the approach in Fig. 4, the local regression rates are compared to the concerning reference case. For illustrative purposes, the virtual grain length (118 mm) of the ULB campaign is indicated in yellow. This way, the significant grain length difference of the two campaigns becomes apparent.

As for the BFS regression rate profile in Fig. 15, the reference and the stepped case before the step are almost identical, confirming that the BFS does have a negligible effect of the regression rate upstream the step. Behind the step, however, the two competing mechanisms of a flow induced by a BFS can be evaluated. Directly after the step, the boundary layer – and therefore the flame – is further away from the grain surface (recalling also Fig. 7). As heat transfer to the fuel surface is the driving mechanism in hybrid fuel regression [4,33], the regression rate of the BFS case is well below the reference cases up until approximately 25 mm after the step. Starting from there, on the other hand, the increased mixing and turbulence induced by the recirculation zone of the step increases the heat transfer from the flame to the surface and the boundary layer re-attaches again. Due to this, a very consistent and high increase in regression rate for the rest of the fuel grain is

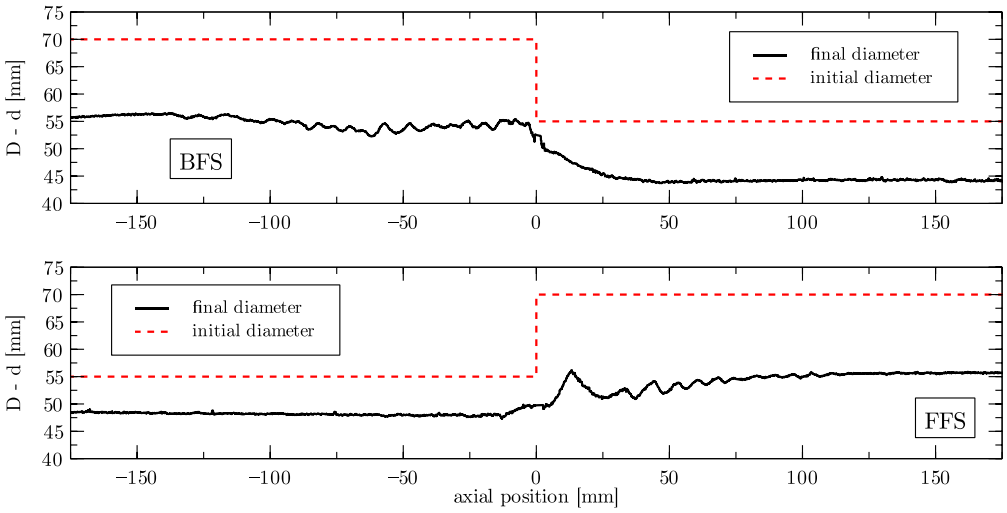

Fig. 14. Initial vs. final diameter for HYCAT cases.

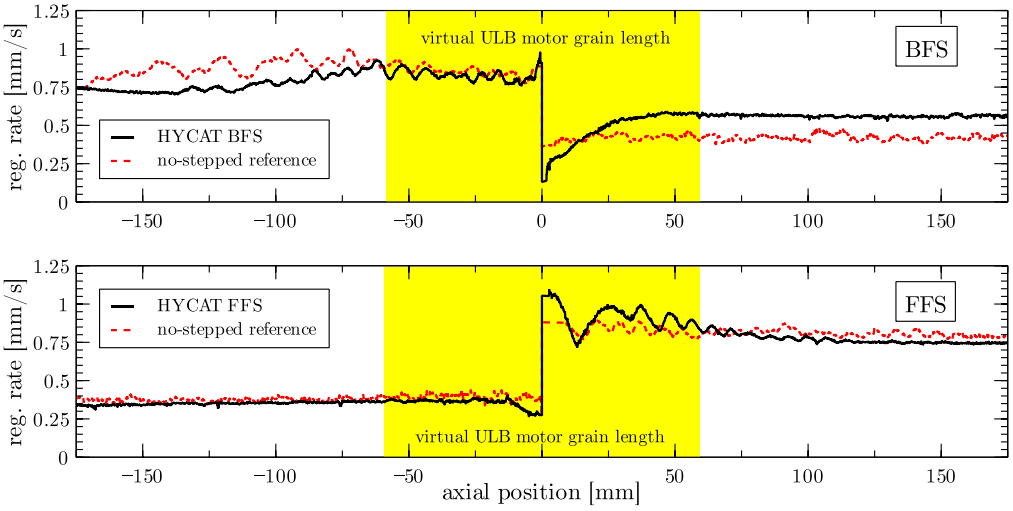

Fig. 15. Regression rate profiles for HYCAT cases. (For interpretation of the references to colour in this figure legend, the reader is referred to the web version of this article.)

observed. Interestingly, this effect appears not to decrease with distance from the step.

Looking at the FFS case at the bottom of Fig. 15, again, the regression rate before the step and the reference are almost identical. However, shortly before the step, the regression rate drops below the reference case. This behaviour is directly opposite to what we observed for the ULB campaign, where the area before the FFS exhibited higher regression rates than the reference. The reason for this different behaviour can be explained with the competing mechanisms in which FFS influence the regression rate of hybrids (keeping in mind Fig. 10). As explained above, a step pushes the flame and boundary layer away from the surface, therefore limiting the heat on the grains surface. However, also due to the step, a recirculation zone develops that increases the mixing and the turbulence and, hence, the regression rate. For the FFS cases of ULB the latter effect seems to be dominating, for HYCAT, however, the first effect has the highest impact.

An explanation for this is can be the following: the average oxidizer mass flux for the ULB campaign for the FFS cases lies around 150 kg/m^2 s, for HYCAT it lies in the order of magnitude of 300 kg/m^2 s. In a numerical study on the HYCAT motor [3], it has been shown that the recirculation zone before the FFS decreases with increasing mass flux. Therefore, the recirculation zone before the FFS is supposed to be bigger for ULB than for HYCAT. Hence, the effect of increased mixing and turbulence is more pronounced than the effect of the flame being further away from the grain surface. Thus, the regression rate for the ULB FFS increases before the step, whereas for HYCAT, it decreases. Confirmation on this hypothesis can be found in [15]. There, the authors conducted studies on diaphragms at mass fluxes between 30–120 kg/m^2 s (therefore closer to our ULB campaign). They inspected the burned fuel grains using X-ray and for all cases (single and multi-protrusion) it was clearly visible that the regression rate before the diaphragm was significantly increased.

However, downstream the FFS, the regression rate of the HYCAT FFS case in Fig. 15 follows the same trend that was observed during the ULB campaign. The increase in regression rate is very pronounced but locally limited. Downstream the FFS, the regression rate approaches the reference case asymptotically.

In yellow, we highlighted the virtual length of an ULB grain (118 mm) to put it into perspective with the HYCAT grain (500 mm). The interesting observation is that for the BFS cases, the ULB grain length does only cover a portion of the regression rate benefit of the BFS. For the HYCAT grain, the regression rate remains increased throughout the remainder of the fuel grain. A first confirmation on the importance of fuel grain length. On the other hand, for the FFS, the virtual ULB grain length falls exactly in the area of increased regression rate. After this length, the HYCAT motor does not profit from

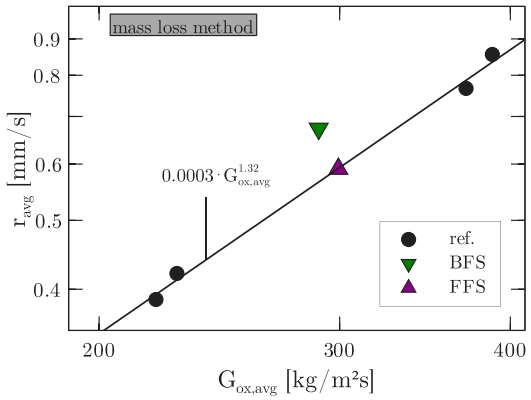

Fig. 16. Space and time averaged regression rate of HYCAT.

any increased regression rate. This is the second proof of importance on grain length. In the next section, this relation is examined more in-depth.

4.4.2. Time and space averaged regression rate for HYCAT campaign

Fig. 16 displays the time and space averaged regression rate obtained with the mass loss method presented in Section 3.1. The Marxman fit for the reference cases is plotted against the FFS and BFS test respectively. The first observation is that contrary to the ULB campaign, the BFS is superior to the FFS. Concerning the BFS, the regression rate is around 26.3% higher than the reference, while for the FFS, the overall regression rate did not increase measurably. Recalling the ULB campaign where the FFS increased the regression rate by 41%, this is an unexpected result.

We postulate two main reasons for the discrepancy in trend and values of increased regression rates for both campaigns. The first, very practical difference is the relation between step height and total fuel grain length for both campaigns. For ULB, the fuel is 118 mm long with a step of 10 mm, which is around 8.5% of the total grain length. Looking at HYCAT, on the other hand, the fuel grain is 500 mm in length with a step of 7.5 mm. This translates to only 1.5% of the fuel length. Considering this, the 26.3% regression rate increase of the BFS in HYCAT is substantial.

While this relative step height–length difference might explain the contrast in absolute values of the regression augmentation, it does not explain why for the ULB motor the FFS is superior to the BFS and exactly opposite with HYCAT. As we already introduced in the preceding section, the explanation for this can be found in the fuel grain length:

1. Inside an HRE, a BFS first decreases the regression rate and then increases it constantly over the remaining fuel grain length. The BFS cases therefore profit from long fuel grains after the step where the constant raise of regression rate accumulates with increasing grain length. This is the case for HYCAT.
2. For the FFS the increase is more pronounced than for BFS but very limited in its area of influence. An effect that is beneficial for shorter grains such as the ones of ULB, where the regression rate peak after the FFS can lie in the order of magnitude of the remaining fuel grain length.

This behaviour was already postulated numerically [3], where the BFS cases in the concerning study benefited from a step position as far upstream as possible due to the constant increase in regression rate after the BFS. In the present work, we are now able to prove this assumption experimentally with the following approach. Let us consider the regression rate profiles for the HYCAT grains in Fig. 15. We already highlighted the virtual length of ULB inside the HYCAT profiles in yellow. Thanks to the slicing method, we can obtain the local regression rate profiles along the fuel grain surface. Using this, we can theoretically integrate the averaged regression rate over any interval of interest (and therefore any simulated fuel grain length) using Eq. (4). Therefore, we integrated the regression rate profiles over three different virtual lengths: (a) the full 500 mm HYCAT length, (b) the 118 mm ULB grain length and (c) an even shorter fuel grain of 50 mm length as example. This approach is depicted in Fig. 17.

Here, the importance of the grain length becomes clearly visible. For the full HYCAT length (left image), the BFS is largely superior to the FFS. Looking at the ULB length of 118 mm displayed in the middle, the BFS and FFS have almost the same effect on the regression rate. Decreasing the integrated virtual fuel grain length further down to 50 mm, as displayed in the right image of Fig. 17, the FFS surpasses the BFS case. This confirms the aforementioned difference in characteristics for the BFS and FFS.

Summarizing the experimental cylindrical studies of ULB and HYCAT, it can be said that qualitatively the local regression rate profiles of the two campaigns yielded the same results, proving that the underlying mechanisms of BFS and FFS are valid over a wide range of initial conditions and grain geometries. However, the question which type of step is more powerful to increase the regression rate remains a strong dependence on the total fuel grain length and its relation to the step height. In short, long grains benefit from average regression rate enhancement through BFS, whereas short grains exhibit higher average regression rates with FFS. Knowing this, the proposal to distribute a set of BFS and FFS along a predefined profile becomes interesting, as many smaller, shorter FFS could be increasing the regression rate more than fewer and bigger BFS.

5. Stepped geometries on two-dimensional slab burner

In the previous sections, we concentrated the investigation of stepped designs on cylindrical cases only. While these configurations are closest to a real use-case, the influence of the steps on the flow and most importantly the regression rate can only be assessed after the tests. That is why for the following sections we investigate the effect of BFS and FFS in the MOUETTE (*Moteur OptiqUe pour ETudier et Tester Ergols hybrides*) slab burner with optical access at ULB. In total, two BFS and two FFS cases were assessed with a step height of 10 mm.

5.1. MOUETTE test facilities

The ULB-ATM MOUETTE hybrid rocket slab burner, shown in Fig. 18, has been developed to investigate the internal ballistics of hybrid rockets. The system operates with gaseous oxygen as oxidizer and paraffin as fuel. The mass flow rate can be increased up to 100 g/s, with a maximum chamber pressure of 10 bar. The test bench is equipped with pressure transducers and K-type thermocouples in the feed system and in the chamber. The combustion behaviour can be monitored with a high-speed camera, taking advantage of two optical accesses, which allows performing both chemiluminescence and for the future Schlieren techniques to acquire experimental data. The length of the fuel grain used in the campaign is 110 mm with a maximum height of 30 mm and 40 mm width. A detailed description of the features of the burner, its design process and capabilities is given in Ref. [7].

5.2. Visual assessment of stepped geometries

The BFS and FFS paraffin slabs mounted in the combustion chamber before the test are displayed in Fig. 19. An overview on the experimental data is given in Table 5. The instantaneous flow-field over the stepped geometries taken from the high-speed camera can be seen in Fig. 20. As a visual support, the silhouette of the respective step is suggested with white lines. For the first pair of BFS and FFS (M1 and M2) the CH* filter is used to detect the emissions of the CH

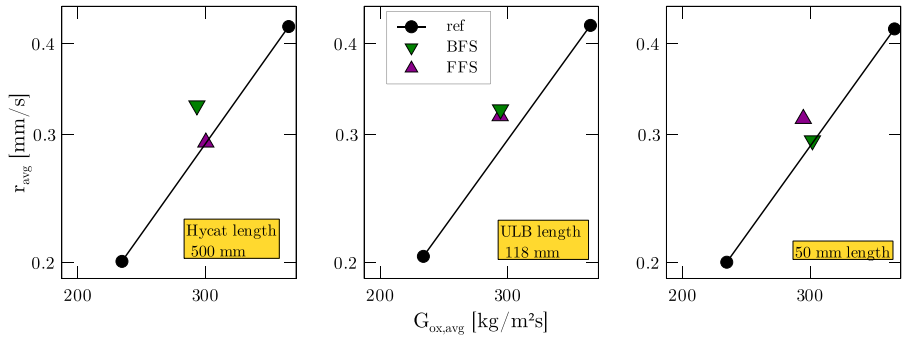

Fig. 17. Length study of space time averaged regression rates.

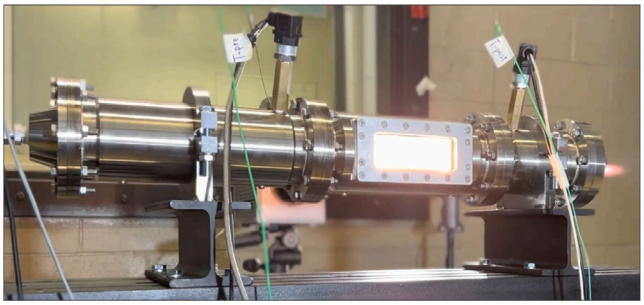

Fig. 18. MOUETTE slab burner with optical access [7].

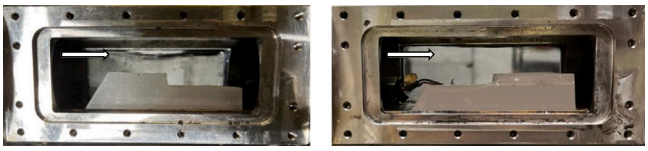

Fig. 19. Paraffin slabs mounted in the combustion chamber.

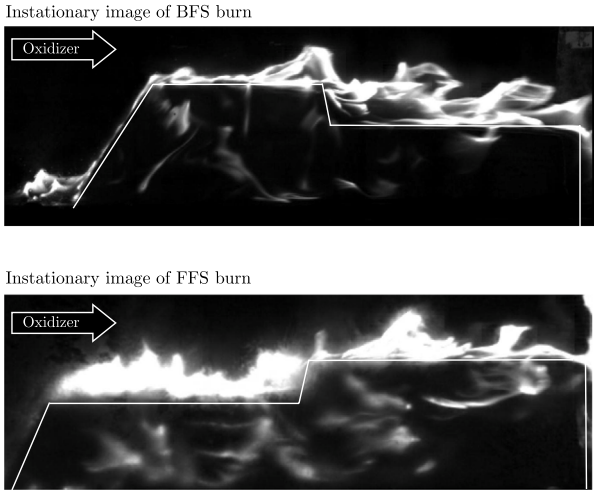

Fig. 20. Instantaneous CH* images of BFS and FFS.

radical (431 nm) which can be directly interpreted as the chemical reaction and heat release zone [34]. Additionally, the second pair of BFS and FFS (M3 and M4) were filmed without filter, therefore capturing the full visible light spectrum. The qualitative images of both the camera with or without filter were identical, that is why we only discuss the images obtained with the CH* filter. One reason for the

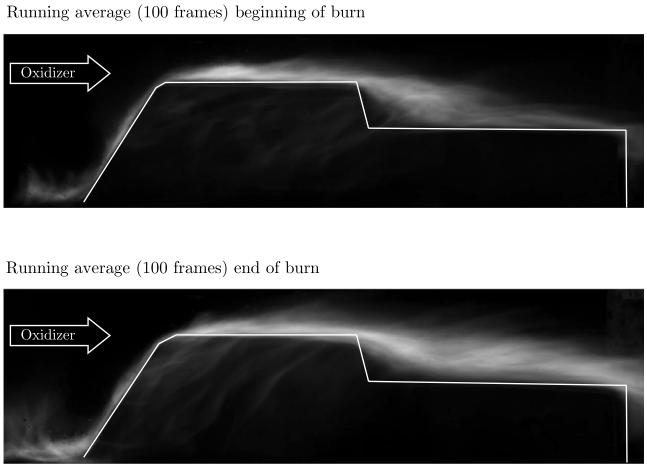

Fig. 21. Running average of BFS case.

Table 5
Overview of MOUETTE test conditions.

Name	Type	Burn time [s]	Chamber pressure [barg]	Mass flow [g/s]
M1	BFS	5.46	2.48	79.20
M2	FFS	7.24	3.33	95.85
M3	BFS	6.10	5.13	95.85
M4	FFS	6.20	5.29	95.85

images with and without filter being qualitatively identical is the fact that the combustion in hybrid rockets is defined by a thin diffusion flame (typically 10% of the boundary layer height [26,33]). Thus, the chemical reaction zone and the hot zone (which emits in the full visible spectrum) are superposed.

Although some flow characteristics can be already guessed from the high-speed images in Fig. 20, due to the turbulent nature of the combustion, it is difficult to assess the details of the flow-field. For this reason, we apply a method to average the turbulence of the combustion. Therefore, the full video is separated into frames (approximately 3000) and the frames are averaged using a moving average for each 100 frames. Using this process, the turbulent behaviour of the combustion can be smoothed out. In Fig. 21, the moving average of the BFS case at the beginning and at the end of the burn is documented. As can be observed, the characteristics of the flow become more visible thanks to the moving average. At the beginning of the flow (upper part), the turbulent boundary layer is clearly visible and the first formation of a recirculation zone is noticeable. For the end of the burn (lower part) the recirculation zone is now fully developed and expands its influence over the whole fuel slab.

The same kind of averaged flow-fields are shown in Fig. 22 for the FFS case. Likewise to Fig. 21, the reaction zones become more

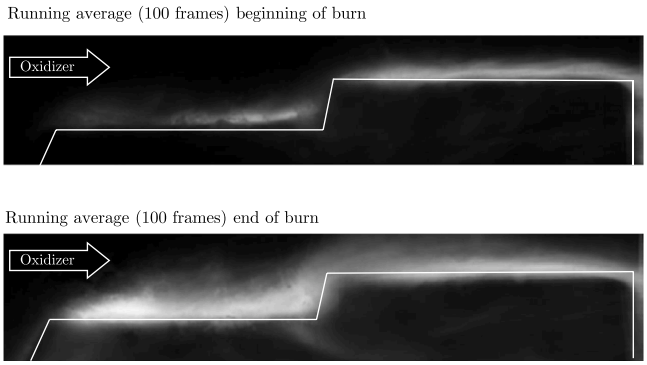

Fig. 22. Running average of FFS case.

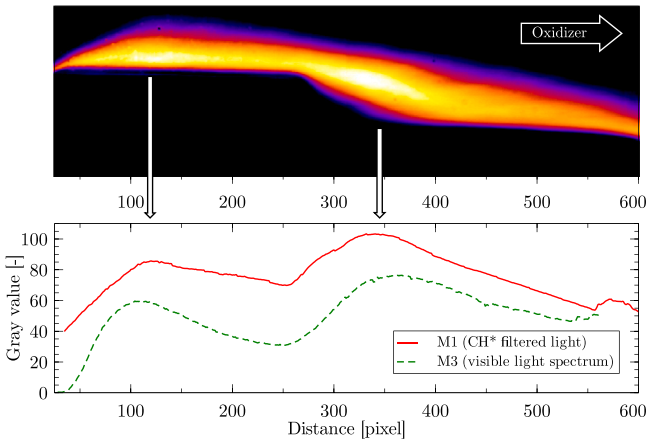

Fig. 23. Intensity profile of BFS case.

visible due to the averaging process. In the upper part of Fig. 22 at the beginning of the burn, the formation of the recirculation zone before and directly after the step can be recognized. Moving to the lower image (representing the end of the burn), both recirculation zones are fully developed, leading to a noisy picture, even after averaging. This hints at a high turbulence level.

While the running averaging method already allows us to better understand the flow-field, to fully resolve the flow-field characteristics over the stepped fuel slabs, a second method is applied. The regression rate of HREs is directly dependent on the fuel surface temperature and therefore the heat transfer from the flame to the fuel surface [26,33]. Thus, higher turbulence levels and recirculation zones locally increase regression rates. Enhanced regression rates lead to augmented combustion and therefore higher CH* intensity. The same reasoning can be also applied vice-versa: because of augmented combustion – visible through the increased CH* intensity – the heat transfer to the surface is augmented and, thus, the regression rate increases. This presents a classic 'causality dilemma'. Nonetheless, in both cases, the intensity of each frame can be used to derive zones of higher regression rates and combustion activity. Jens et al. [35] have found a direct proportionality between chemiluminescence intensity and (global) regression rates for both classic and paraffin based fuels in their hybrid slab burner. Jens et al. [35] used OH* chemiluminescence, but it has been shown that CH* and OH* curves are very similar in shape and peak position [34].

Instead of averaging each frame, we total the gray value (representing the CH* intensity) of each pixel in each frame during the burn time along the y-axis. This allows to detect zones of higher chemical reaction. With this information, we can connect the zones of higher intensity directly to areas with higher turbulence and regression rates. For the second set of BFS and FFS tests (M3 and M4), we deliberately omitted the CH* filter in order to evaluate the necessity of a filter to assess regions of increased regression rates. The process to obtain the intensity profiles is described in Eq. (10):

$$I(x) = \frac{1}{y_{\max}} \sum_{y=0}^{y_{\max}} \sum_{t=t_{\text{ign}}}^{t_{\text{burn}}} \frac{I(x,y,t)}{t_{\text{burn}}}, \tag{10}$$

with I being the Intensity or gray value, $y_{\max}$ the maximum frame height and t_{burn} and t_{ign} the burn and ignition time, respectively. Using Eq. (10), an intensity profile along the x-axis can be calculated which is presented in Fig. 23 for the BFS cases. Additionally, the summarized intensity of the image is represented on the upper half of the image, allowing to relate the flow phenomena directly to the derived intensity curves of Eq. (10). It is to be noted that the upper part of Fig. 23 shows only the flow-field obtained with the CH* filter of M1. Because the resulting images for M3 in the visible light were identical, they are not shown here again in order to condense the information into one single figure. The bottom parts of the images, however, plot the intensity curves for both M1 and M3. Looking at Fig. 23, as anticipated, the peaks of the intensity profile correlate exactly to the areas of recirculation and increased turbulence and, thus, higher regression rates. The first peak of the intensity curves is explained recalling Fig. 19. The way the grain holder of MOUETTE is designed, each fuel slab consists of a rather dominant step at the beginning of the grain (for a detailed reasoning into the design choices of the grain holder and MOUETTE in general, the reader is referred to [7]). Since this BFS at the beginning of the fuel grain induces a recirculation zone – similar to the step in the middle of the fuel grain – a distinct peak is noticeable at the beginning of the fuel grain. The second peak of the intensity can be found not far downstream from the main step in the middle. This correlates closely to what we observed for the cylindrical BFS cases in Figs. 8 and 15 and supports the theory that the intensity can be used as a qualitative indicator for increased regression rates.

Interestingly, the qualitative results for the intensity curves with CH* filter (M1) and with all visible light (M3) follow the exact same trend. This signifies that the increased chemical reactivity for the areas of higher combustion is not only reflected in the intensity profiles of the CH* but also in the full visible spectrum. This was to be expected, as CH emits in the visible light. The reason that the absolute intensity values of the visible light curve is lower than the CH* curve is due to the fact that the camera used does not allow for quantitative analyses. As soon as the setup is varied, the absolute gray values change too. Additionally, the shutter opening time for the cases recording the full visible spectrum had to be decreased by a factor of 100 as compared to the CH* filter recordings to avoid over-exposure of the images. This leads to less bright images for the tests of M3 and M4, but qualitatively the trend of the CH* filtered and unfiltered intensity curves are identical.

The same intensity approach is followed for the FFS cases and is depicted in Fig. 24. Again, it is evident that the intensity profiles of the visible light and the CH* filter are strongly correlated as explained above. Moreover, the observations of the intensity plots are in line with the behaviour of the cylindrical fuel grains of ULB in Fig. 11.

Three peaks in intensity are distinguishable. The first peak is due to the same phenomena that was explained for the BFS MOUETTE cases. The beginning of the fuel slab consists of a step, therefore triggering a recirculation zone. The second peak lies directly before the FFS. Recalling Fig. 11 of the ULB FFS study, the behaviour of the slab burner and ULB motor are identical, as for both cases, the regression rate immediately before the FFS is augmented.

Interestingly, HYCAT did not exhibit this small area of increased regression rate before the step as discussed in Section 4.4.1. We analysed this to be due to the relatively high G_{ox} values of HYCAT (200–400 kg/m^2 s). Compared to HYCAT, the G_{ox} values of MOUETTE are substantially smaller (around 20 kg/m^2 s). This supports the theory that the initial peak before a FFS preferably occurs for lower G_{ox} values. The third, less pronounced peak can be derived from the recirculation

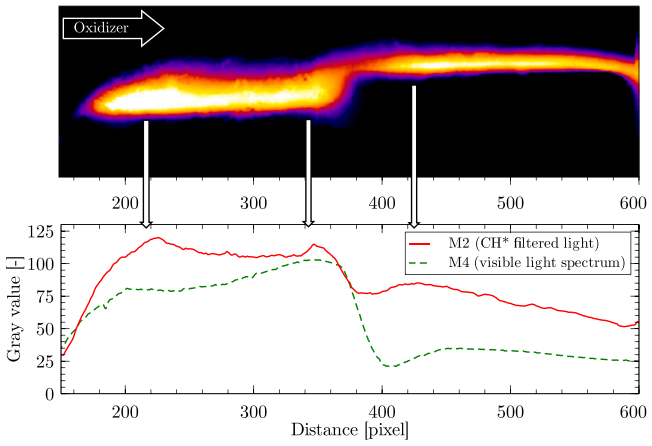

Fig. 24. Intensity profile of FFS case.

zone directly after the FFS. Likewise to both cylindrical campaigns, the regression rate shortly after the FFS is elevated.

To conclude, we observed the same physical phenomena as the experimental results of the cylindrical campaigns using image processing. Moreover, we have shown that the effect of steps can be reproduced also for 2D geometries and using paraffin instead of HDPE. This justifies the use of slab burners with visual access to further investigate the effect of stepped geometries on the regression rate in the future. Additionally, the presented optical investigation of regression rates can be used on longer tests to directly derive the evolution in combustion zone and the geometry of the fuel, thus allowing to observe the progression of the step(s) over time. One possible adjustment to the experimental set-up would be to use longer fuel grains to eliminate the effect of the first step at the onset of the fuel grain or decreasing the angle of attack of the fuel slabs at the beginning.

6. Concluding remarks

In this work, the positive effects of BFS and FFS inside HREs have been shown experimentally on two different lab-scale motors and one slab burner with optical access. Although the propellant couple of the cylindrical motors of the ULB and HYCAT campaigns was different, the qualitative results of the local regression rate profiles were identical, but showed differences in the space and time averaged regression rates. For the ULB motor, the FFS increased the average regression rate 41.3% above the reference trend line, in the case of BFS the increase was 15.7%. Surprisingly, for the HYCAT motor, the trend was reversed. The BFS case of HYCAT increased the overall regression rate by 26.3%, whereas the FFS had an negligible effect on the time and space averaged regression rate. Thanks to detailed investigations of the regression rate profiles along the surface of the fuel grain, the areas of locally increased regression rates could be qualitatively and quantitatively assessed, allowing to explain the observed results. The deciding difference between ULB and HYCAT concerning the employment of steps is not the different propellant couple but the total fuel grain length (and to a lesser extent the ratio of total fuel grain length to step height). With the help of the regression rate profiles, we derived the following considerations explaining the behaviour of the steps:

1. For BFS, the locally increased regression rate is mostly confined to downstream the step position. After the step, the regression rate is increased by a considerable amount over the reference. This augmentation remains valid over the remainder of the fuel grain. For this reason, longer fuel grains profit more from BFS than from FFS. Based on the local regression rate profiles of both cylindrical campaigns, we anticipate that a potential second BFS (or FFS for that matter) should be placed at around 30 mm downstream the BFS which correlates to 3 times the step height for the ULB campaign. Up to this length-to-height ratio of 3, the local regression rate continues to increase, until it slowly starts descending (refer also to Fig. 8). As for HYCAT, the optimal length could be extended to 75–100 mm, translating to a ratio of 10–13, potentially even higher, given the constant increase of regression rate (recall also Fig. 15).
2. For the FFS cases, the regression rate enhancement is almost exclusively noticeable directly after the step, but very pronounced. After the step, for the ULB campaign, the increased regression rate profiles are measurable until approximately 20 mm after the step yielding a length-to-height ratio of 2. For the almost 4.5 times longer HYCAT grains, the increasing effect after the FFS ends at around 50 mm (length-to-height ratio 6–7) downstream the step. This explains why shorter grains benefit more from FFS, and longer grains show – averaged over the whole fuel grain length – a negligible effect of FFS. The single, distinct peak of 50 mm width after the FFS is too small to be measurable for a grain length of 500 mm. For the ULB campaign, the area of influence of the FFS (50 mm) is considerably higher relative to the fuel grain length (only 118 mm). Translating these considerations to potential multiple steps, it is postulated that distributing multiple FFS in longer fuel grains can add up their individual zone of influence to also have considerable effect on the space and time averaged regression rates.

As for the 2D slab burner campaign, it has been shown that the effects of steps are also existing for paraffin fuels and in the two-dimensional domain. Using image post-processing through the optical access of the slab burner, the areas of higher regression rates could be already identified during the burn through an analysis of the CH* and visible light intensity. These areas of the 2D campaign correspond to both cylindrical test campaigns that use HDPE. This allows us in the future to investigate the instantaneous regression of the steps with time more conveniently through an optically accessible slab burner like MOUETTE, even without the necessity of CH* filters (or any other type of filter).

Future work has to prove whether the beneficial effect of a single BFS or FFS can be accumulated by using multiple BFS and FFS (be it in alternating fashion or by steps of the same type), or whether a saturation on the regression rate augmentation will be obtained at some point. Another field of interest is the influence of BFS and FFS on pressure oscillations and combustion efficiency. With the help of a piezoelectric pressure transducer, the impact of the steps on the chamber pressure will be assessed in the future. We expect, based on the study of Lee et al. [17], that pressure oscillation are less a concern for the BFS cases and more for the FFS cases. FFS resemble diaphragms in the fuel port that usually trigger pressure oscillations in HREs. Preliminary investigations on our cylindrical test campaigns, however, suggest that neither the FFS nor the BFS seem to induce noteworthy instabilities.

Concluding this work, the feasibility of BFS and FFS and their potential to increase the regression rate in HREs have been proven on three different experimental set-ups. For the future, the combination of multiple steps needs to be evaluated, especially the interaction of a FFS and BFS is of high interest as well as building a larger experimental data base. With these data, finally, a fully stepped fuel port profile can be designed and evaluated numerically and experimentally.

Declaration of competing interest

The authors declare that they have no known competing financial interests or personal relationships that could have appeared to influence the work reported in this paper.

Acknowledgements

The authors would like to thank the technical experts (Olivier, Yves, Lionel, Charly and Florent) at ULB-ATM for their support before and after the experimental test campaigns of the ULB and MOUETTE motors, and Laurent at ULB for his expertise in data acquisition. We are thankful for the Belgian Air Force in Beauvechain for hosting our test campaign(s). From the side of ONERA Fauga-Mauzac we want to express our gratitude to the technical team (Sébastien, Cédric, Jean-Charles and Christophe) for their support before, during and after the HYCAT test campaign.

Funding

The project leading to this application has received funding from the European Union's Horizon 2020 research and innovation programme under the Marie Sklodowska-Curie grant agreement No 860956. It is part of the ASCenSIon project, an Innovative Training Network (ITN) to advance space access capabilities (https://ascension-itn.eu/). A. E. M. Bertoldi received funding from the Marie Sklodowska-Curie grant agreement No 801505.

References

[1] K. Kuo, M. Chiaverini, Challenges of hybrid rocket propulsion in the 21st century, in: Fundamentals of Hybrid Rocket Combustion and Propulsion, American Institute of Aeronautics and Astronautics, Reston, Virginia, 2007, pp. 593–638, http://dx.doi.org/10.2514/5.9781600866876.0593.0638.

[2] A. Okninski, W. Kopacz, D. Kaniewski, K. Sobczak, Hybrid rocket propulsion technology for space transportation revisited - propellant solutions and challenges, FirePhysChem (2021) http://dx.doi.org/10.1016/j.fpc.2021.11.015.

[3] C. Glaser, J. Hijlkema, J. Anthoine, Approximating idealized hybrid rocket fuel port geometries using steps, in: 8th Edition of the Space Propulsion Conference, Portugal, 2022.

[4] C. Glaser, R. Gelain, A. Bertoldi, J. Hijlkema, P. Hendrick, J. Anthoine, Experimental investigation of stepped fuel grain geometries in hybrid rocket engines, 2022, http://dx.doi.org/10.13009/EUCASS2022-4448.

[5] M. Bouziane, A. Bertoldi, P. Milova, P. Hendrick, M. Lefebvre, Performance comparison of oxidizer injectors in a 1-kN paraffin-fueled hybrid rocket motor, Aerosp. Sci. Technol. 89 (2019) 392–406, http://dx.doi.org/10.1016/j.ast.2019.04.009.

[6] J.-Y. Lestrade, J. Anthoine, O. Verberne, A.J. Boiron, G. Khimeche, C. Figus, Experimental demonstration of the vacuum specific impulse of a hybrid rocket engine, J. Spacecr. Rockets 54 (1) (2017) 101–108, http://dx.doi.org/10.2514/1.a33467.

[7] R. Gelain, F. Angeloni, A.E. De Morais Bertoldi, P. Hendrick, Design and commissioning of the MOUETTE hybrid rocket slab burner, in: 9th European Conference for Aeronautics and Space Sciences (EUCASS), 2022.

[8] C. Glaser, J. Hijlkema, J. Anthoine, Evaluation of regression rate enhancing concepts and techniques for hybrid rocket engines, Aerotecn. Missili Spazio (2022) http://dx.doi.org/10.1007/s42496-022-00119-4.

[9] C. Carmicino, A.R. Sorge, Role of injection in hybrid rockets regression rate behaviour, J. Propuls. Power 21 (4) (2005) 606–612, http://dx.doi.org/10.2514/1.9945.

[10] C. Carmicino, A.R. Sorge, Influence of a conical axial injector on hybrid rocket performance, J. Propuls. Power 22 (5) (2006) 984–995, http://dx.doi.org/10.2514/1.19528.

[11] F. Shan, L. Hou, Y. Piao, Combustion performance and scale effect from N2O/HTPB hybrid rocket motor simulations, Acta Astronaut. 85 (2013) 1–11, http://dx.doi.org/10.1016/j.actaastro.2012.12.013.

[12] P. Duban, La fusée sonde LEX, in: Extrait de L'AÉRonautique Et L'Astronautique, 1968.

[13] A. Gany, Y. Timnat, Parametric study of a hybrid rocket motor, Isr. J. Technol. 10 (1972) 85–96.

[14] M. Grosse, Effect of a diaphragm on performance and fuel regression of a laboratory scale hybrid rocket motor using nitrous oxide and paraffin, in: 45th AIAA/ASME/SAE/ASEE Joint Propulsion Conference and Exhibit, American Institute of Aeronautics and Astronautics, Reston, Virginia, 2009, http://dx.doi.org/10.2514/6.2009-5113.

[15] M. Dinesh, R. Kumar, Utility of multiprotrusion as the performance enhancer in hybrid rocket motor, J. Propuls. Power 35 (5) (2019) 1005–1017, http://dx.doi.org/10.2514/1.B37491.

[16] P.A.O.G. Korting, H.F.R. Schöyer, Y.M. Timnat, Advanced hybrid rocket motor experiments, Acta Astronaut. 15 (2) (1987) 97–104, http://dx.doi.org/10.1016/0094-5765(87)90009-9.

[17] J. Lee, S. Rhee, J. Kim, H. Moon, Combustion instability mechanism in hybrid rocket motors with diaphragm, J. Propuls. Power (2021) 1–10, http://dx.doi.org/10.2514/1.B38492.

[18] H. Sakashi, Y. Saburo, H. Kousuke, S. Takashi, Effectiveness of concave-convex surface grain for hybrid rocket combustion, in: 48th AIAA/ASME/SAE/ASEE Joint Propulsion Conference and Exhibit, 2012, http://dx.doi.org/10.2514/6.2012-4107.

[19] M. Kumar, P. Joshi, Regression rate study of cylindrical stepped fuel grain of hybrid rocket, Mater. Today: Proc. 4 (8) (2017) 8208–8218, http://dx.doi.org/10.1016/j.matpr.2017.07.163.

[20] L. Kamps, K. Sakurai, Y. Saito, H. Nagata, Comprehensive data reduction for N2O/HDPE hybrid rocket motor performance evaluation, Aerospace 6 (4) (2019) http://dx.doi.org/10.3390/aerospace6040045.

[21] H. Nagata, M. Ito, T. Maeda, M. Watanabe, T. Uematsu, T. Totani, I. Kudo, Development of CAMUI hybrid rocket to create a market for small rocket experiments, Acta Astronaut. 59 (1) (2006) 253–258, http://dx.doi.org/10.1016/j.actaastro.2006.02.031.

[22] H. Tian, X. Sun, Y. Guo, P. Wang, Combustion characteristics of hybrid rocket motor with segmented grain, Aerosp. Sci. Technol. 46 (2015) 537–547, http://dx.doi.org/10.1016/j.ast.2015.08.009.

[23] Y. Nobuhara, L.T. Kamps, H. Nagata, Fuel regression characteristics of CAMUI type hybrid rocket using nitrous oxide, in: AIAA Propulsion and Energy 2021 Forum, American Institute of Aeronautics and Astronautics, Reston, Virginia, 2021, http://dx.doi.org/10.2514/6.2021-3521.

[24] A. Karabeyoglu, G. Zilliac, B.J. Cantwell, S. DeZilwa, P. Castellucci, Scale-up tests of high regression rate paraffin-based hybrid rocket fuels, J. Propuls. Power 20 (6) (2004) 1037–1045, http://dx.doi.org/10.2514/1.3340.

[25] J. Schindelin, I. Arganda-Carreras, E. Frise, V. Kaynig, M. Longair, T. Pietzsch, S. Preibisch, C. Rueden, S. Saalfeld, B. Schmid, J.-Y. Tinevez, D.J. White, V. Hartenstein, K. Eliceiri, P. Tomancak, A. Cardona, Fiji: an open-source platform for biological-image analysis, Nature Methods 9 (7) (2012) 676–682, http://dx.doi.org/10.1038/nmeth.2019.

[26] G. Marxman, M. Gilbert, Turbulent boundary layer combustion in the hybrid rocket, Symp. (Int.) Combust. 9 (1) (1963) 371–383, http://dx.doi.org/10.1016/s0082-0784(63)80046-6.

[27] M.A. Karabeyoglu, B.J. Cantwell, G. Zilliac, Development of scalable space-time averaged regression rate expressions for hybrid rockets, J. Propuls. Power 23 (4) (2007) 737–747, http://dx.doi.org/10.2514/1.19226.

[28] M. Bouziane, A.E. De Morais Bertoldi, P. Milova, P. Hendrick, M. Lefebvre, Development and testing of a lab-scale test-bench for hybrid rocket engines, in: SpaceOps Conferences, American Institute of Aeronautics and Astronautics, 2018, http://dx.doi.org/10.2514/6.2018-2722.

[29] M.A. Karabeyoglu, D. Altman, B.J. Cantwell, Combustion of liquefying hybrid propellants: Part 1, general theory, J. Propuls. Power 18 (3) (2002) 610–620, http://dx.doi.org/10.2514/2.5975.

[30] D. Bianchi, F. Nasuti, Numerical analysis of nozzle material thermochemical erosion in hybrid rocket engines, J. Propuls. Power 29 (3) (2013) 547–558, http://dx.doi.org/10.2514/1.B34813.

[31] T. Hui, Y. Ruipeng, L. Chengen, Z. Sheng, Z. Hao, Numerical and experimental study of the thermochemical erosion of a graphite nozzle in a hybrid rocket motor with a star grain, Acta Astronaut. 155 (2019) 10–22, http://dx.doi.org/10.1016/j.actaastro.2018.11.007.

[32] J.-É. Durand, F. Raynaud, J.-Y. Lestrade, J. Anthoine, Turbulence modeling effects on fuel regression rate in hybrid rocket numerical simulations, J. Propuls. Power 35 (6) (2019) 1127–1142, http://dx.doi.org/10.2514/1.b37528.

[33] T. Marquardt, J. Majdalani, Review of classical diffusion-limited regression rate models in hybrid rockets, Aerospace 6 (6) (2019) 75, http://dx.doi.org/10.3390/aerospace6060075.

[34] Y. Liu, J. Tan, H. Wang, L. Lv, Characterization of heat release rate by OH* and CH* chemiluminescence, Acta Astronaut. 154 (2019) 44–51, http://dx.doi.org/10.1016/j.actaastro.2018.10.022.

[35] E.T. Jens, V.A. Miller, B.J. Cantwell, Schlieren and OH* chemiluminescence imaging of combustion in a turbulent boundary layer over a solid fuel, Exp. Fluids 57 (3) (2016) 39, http://dx.doi.org/10.1007/s00348-016-2124-x.